Materials & Design 210 (2021) 110122

Contents lists available at ScienceDirect

Materials & Design

journal homepage: www.elsevier.com/locate/matdes

Comparative study of deposition patterns for DED-Arc additive manufacturing of Al-4046

Markus Köhler [a,*], Li Sun [b,*], Jonas Hensel [a], Sakari Pallaspuro [c], Jukka Kömi [c], Klaus Dilger [a], Zhiliang Zhang [b,*]

[a] Institute of Joining and Welding, Technische Universität Braunschweig, Langer Kamp 8, 38106 Braunschweig, Germany
[b] Department of Structural Engineering, Norwegian University of Science and Technology, Trondheim 7491, Norway
[c] Materials and Mechanical Engineering, University of Oulu Centre for Advanced Steels Research, P.O. Box 4200, FI-90014 University of Oulu, Finland

HIGHLIGHTS

- The relationship between deposition patterns and their characteristics is revealed.
- Porosity and microstructure depend on local peak temperature and temperature gradient.
- Residual stresses are related to the uniformity of global temperature distribution.
- The S pattern produces smaller coarse-grain size, less porosity, and lower residual stress.

GRAPHICAL ABSTRACT

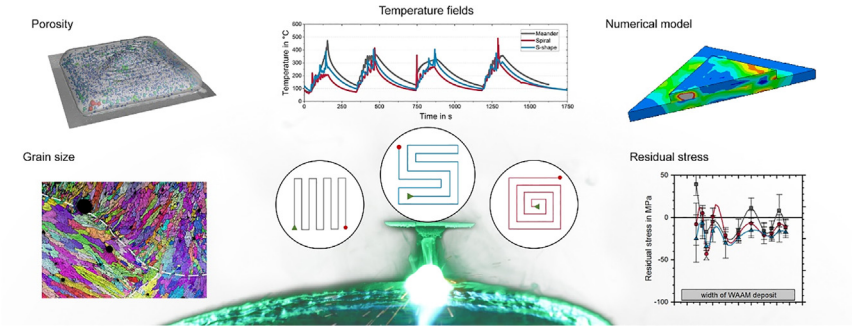

ARTICLE INFO

Article history:
Received 5 July 2021
Revised 3 September 2021
Accepted 22 September 2021
Available online 23 September 2021

Keywords:
Wire arc additive manufacturing
Aluminum
Deposition patterns
Residual stress
Porosity
Grain size

ABSTRACT

Quality assurance is one of the largest challenges to the widespread adoption of metal additive manufacturing technology. Deposition pattern can significantly impact the temperature distribution during manufacturing process and thus the overall quality and residual stress formation of the manufactured components. In order to explore the intricate relationship, three different deposition patterns in DED-Arc additive manufacturing, the meander pattern, the spiral pattern and the newly developed S pattern, were experimentally and numerically scrutinized in terms of the resulting temperature distribution, grain size, porosity as well as residual stress formation. The study reveals that the variation of the deposition paths results in characteristic temperature fields and gradients with distinct local peak temperatures that determine the deposition quality, and simultaneously offers great degrees of freedom for optimal pattern design. Comparing the results with different deposition patterns, the S pattern leads to a more homogeneous temperature distribution, showing beneficial effects on the microstructure, porosity and residual stress formation in the deposited Al-4046 material, and is thus regarded as a promising alternative for improving additively manufactured parts quality.

1. Introduction

Recently, there has been a growing interest in advanced manufacturing methods in research and industry. One of the emerging technologies is additive manufacturing of metal components using gas metal arc welding technology [1,2]. DED-arc additive manufac-

* Corresponding authors.
E-mail addresses: markus.koehler@tu-braunschweig.de (M. Köhler), li.sun@ntnu.no (L. Sun), zhiliang.zhang@ntnu.no (Z. Zhang).

https://doi.org/10.1016/j.matdes.2021.110122
0264-1275/

turing also known as wire arc additive manufacturing (WAAM) is considered a disruptive technology that addresses some of the major downsides of laser-powder-based additive manufacturing. The equipment is more robust, the investment cost of equipment and systems is lower, the build-up volume is easily scalable, and the feed material is available in various grades of high quality. Furthermore, the deposition rate compared to single laser processes is higher. On the other hand, the geometric accuracy and surface quality is considerably lower [3].

High deposition rates of WAAM result from a relatively high energy input, which leads to relatively large melt pools, but also to excessive grain growth, which impairs the mechanical properties. Furthermore, the distinctive local thermal gradients during manufacturing, combined with increasing restraint, cause residual stress and distortion. These phenomena are considered as one of the major challenges during WAAM, as they affect material characteristics, post-weld machinability, and the additive manufacturing process itself [4]. Three-dimensional distortion affects process parameters such as the orientation and distance of the welding torch to the work piece. Low accuracy of deposition position may result in high geometric inaccuracy, process instabilities, defects or process interruption. Although some ideas for geometry adaptive path planning exist, pre-planning of build-up strategies and offline programming of WAAM machines are state of the art nowadays [5]. Today, the user of the WAAM technology must therefore trade theoretically possible high deposition rates for lower distortion. This is especially true in case of WAAM of aluminum components due to high thermal conductivity, low Young's modulus and low yield limits of filler wires in the as-built condition.

Based on its physical properties of a high strength-to-density ratio, high thermal and electrical conductivity and good corrosion resistance, aluminum is a commonly used material in a variety of industrial applications such as aerospace, automotive and consumer industries. Due to its unique advantages in terms of material utilization, high deposition rates, freedom of design and the possibility to manufacture independently from the number of components produced, WAAM of aluminum alloys is particularly suitable for the production of complex geometries for large scale light-weight structures as well as for the individualization of semi-finished cast components [6,7]. However, the physical properties of aluminum also present special challenges for gas metal arc welding-related processing during WAAM. The high thermal conductivity and thermal expansion coefficient result in rapid heat dissipation and hence to high temperature gradients and the formation of comparatively high shrinkage strains [8,9]. Further, the high temperature gradients during deposition often result in a softening and coarse grain formation of the heat affected zone [10]. A high difference in the solubility limit of hydrogen during solidification of aluminum is commonly referred to as the main reason for process induced formation of metallurgical porosity [10–12]. Thereby, hydrogen from the process environment and surface contaminations is dissolved in the melt pool and enclosed in the deposition metal during solidification, causing gas porosity. Studies on thin-walled and block WAAM samples show that the quality of WAAM aluminum components in terms of geometrical and mechanical properties as well as porosity formation is determined by the material composition, the process settings and the temperature distribution during deposition [13–18]. To reduce the heat input during deposition, energy reduced short arc processes such as cold metal transfer (CMT) are widely used for WAAM [19,20]. For the processing of Al-alloys, process variations including CMT pulse and CMT advanced have shown beneficial effects with regard to penetration characteristics, microstructural properties and the formation of porosity [14]. Further, the interlayer temperature can affect the deposition properties. For AlMg5, Derekar et al. found an increase in small size pores as well as coarser grain size using higher interlayer temperature, whereas a lower interlayer temperature led to an increase in large size porosity [16].

Besides various influences by the processing technology itself, path planning can have a major influence on the overall quality of WAAM components. According to Liu et al., path planning methods for WAAM can be mainly divided into linear path planning, contour path planning and the combination of aforementioned (see Fig. 1) [4]. Thereby, the raster and zigzag (also referred to as meander) pattern are the most commonly used linear path planning strategies [21]. The raster strategy relies on filling the contour with individual lines. This leads to an easy implementation with limited computing time [22]. However, the high number of single deposition paths can lead to poor contour accuracy and the accumulation of geometrical deviations caused by a high number of arc start/stop-positions [23]. It is further expected that the raster pattern will lead to comparatively high residual stress due to the uniform direction of the deposition paths combined with higher residual stress longitudinal to the deposition direction and at arc start positions [24]. Derived from the raster strategy, the zigzag method combines individual line segments to a continuous meandering shape by alternating the path direction and connecting the lines start- and end-points, thus leading to a significant reduction of arc start/stop-positions [25]. Especially for complex shaped contours with islands and concave geometries, the zigzag method shows a more difficult implementation, leading to a segmentation with multiple meander paths. In order to enhance the contour accuracy and to further reduce the number of arc start/stop-positions for zigzag-based path planning of complex shaped structures, Ding et al. proposed a method in which the geometry is decomposed into convex sub-geometries [21]. By linking the zigzag sub-tool paths, a continuous process was realized. Wang et al. presented an advancement of the zigzag strategy based on a water-pouring method, effectively reducing the number of arc start/stop-positions and improving on the surface uniformity [26]. However, the comparatively long, continuous deposition sequences can lead to constantly increasing component temperatures, depending on the material and process settings, and thus affecting the metallurgical and geometrical properties during deposition. The contour filling strategy is based on an incremental scaling of the outer contour from the initial geometry and results in superior contour accuracy compared to linear path planning strategies [4]. Referring to the contour filling, the spiral pattern is used to reduce the number of individual deposition paths for convex shaped geometries [27]. Due to the contour-offset, based on the width of the deposition bead, contour filling and spiral path planning often result in voids when the geometry does not match an integer multiple of the bead width. For improving geometric accuracy and enabling the manufacturing of void-free parts using contour parallel path planning, Xiong et al. introduced a process planning framework based on variable bead width by adapting the processing parameters [28]. A combination of contour path and linear zigzag fill-in can be used to combine the advantages in terms of contour accuracy and building efficiency. Comparing the residual stress formation in combined zigzag and contour fill-in, Zhang et al. found lower, more uniformed, residual stress in areas with contour patterns due to a more uniform temperature distribution [24]. From this research, it is suggested to use a maximum of contour paths before switching to zigzag pattern in order to minimize residual stress. Su et al. investigated the influence of deposition pattern and interlayer rotation on the resulting microstructure and tensile properties using AlSi5. The results showed comparatively lower grain size and higher tensile strength using raster pattern with 45° interlayer rotation whereas an interlayer rotation of 90° resulted in better ductility [29]. Based on the current state of research, each deposition pattern has its individual advantages and disadvantages in terms of geometrical accuracy

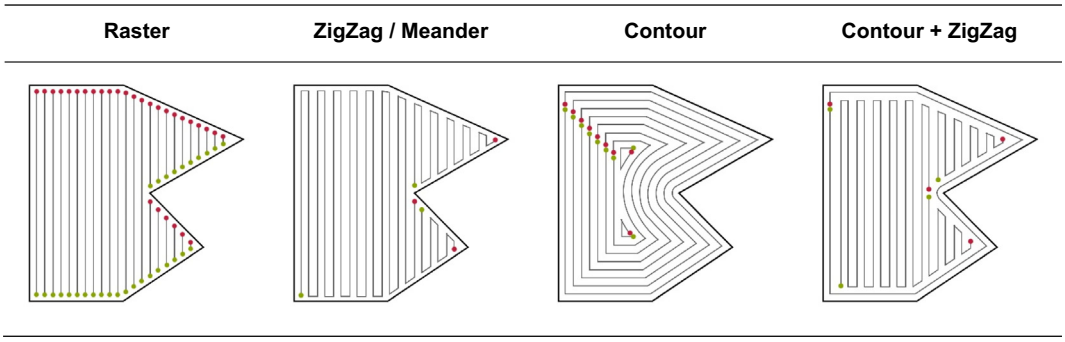

Fig. 1. Example of commonly used deposition patterns for WAAM.

and applicability, mechanical properties as well as production speed. Therefore, the choice in deposition pattern depends on the particular application and quality requirements.

Residual stress and distortion are, to some extent, an unavoidable problem during WAAM of metals due to the high heat input. Especially in case of WAAM using aluminum, the heat input is not arbitrarily reducible due to the high heat conductivity of aluminum alloys and the interconnected tendency to cause lack of fusion of different layers. Since residual stress and distortion affect both the production processes and component abilities in service, such as fatigue strength and corrosion behavior, a better understanding of generation mechanisms is needed, as pointed out by Williams et al. and Gibson et al. [30,31]. The general phenomenon of residual stress generation due to local thermal arc and laser treatments is well understood from many decades of research in welding technology [32,33]. Important analogies are evident in terms of influences from heat input, pre-heating and interlayer temperatures, material characteristics and process management. Many of these parameters were studied with regard to laser-powder AM processes, mainly laser powder bed fusion (LPBF). Mercelis and Kruth observed high residual stress at the interface of substrate and build-up material during laser powder bed fusion, while the magnitude of residual stress is determined by the restraint of the substrate and the clamping [34]. Salmi et al investigated residual stress formation in AlSi10Mg processed by laser powder bed fusion and proved that a lower degree of restraint resulting from a slender substrate or weaker support structures is beneficial [35]. Furthermore, the degree of restraint can be reduced by limiting temperature gradients. Wang et al. demonstrated the positive effect of increased interpass temperatures on residual stress in AlSi10Mg produced by LPBF [36]. Furthermore, the overall geometry of the build part determines the residual stress magnitude and distribution. Tensile residual stress is usually found at the last deposited layers, while the layers at the interface to the substrate are in compression. The substrate itself is often under bending stress as well, with tension at the top surface and compression at the bottom, see research from Colegrove et al. and Hönnige et al [37,38]. Another approach to control the degree of restraint during manufacturing is to homogeneously distribute the heat in the component through adjusted scanning strategies during LPBF. Robinson et al. recently demonstrated this approach and proved the beneficial effect, although residual stress cannot be fully suppressed [39].

This study focuses on the possibility to positively affect residual stress fields, grain size, and porosity by controlling temperature gradients through adaption of deposition patterns during WAAM with AlSi10Mg filler wire. The idea of this work is to minimize temperature gradients within the entire build-up volume by a more homogeneous heat input. Three deposition patterns with continuous deposition processes are investigated in this work: The meander pattern, the spiral pattern and the novel S pattern recently introduced by Sun et al. [40]. Next to residual stress, this study compares the quality of deposition volumes, material irregularities and metallurgy.

2. Materials and methods

2.1. Sample preparation

The experimental robotic-WAAM setup consists of a *KUKA KR-22* 6-axis robotic system with a tilt and turn positioning table coupled with a *Fronius CMT-Advanced 4000* welding power source (Fig. 2 (a)). For the manufacturing of WAAM samples, a custom-made ER4046 solid wire electrode with a diameter of 1.0 mm was used on an EN6062 wrought plate substrate with the dimensions of 120 × 120 × 10 mm^3. The chemical compositions of the materials are provided in Table 1. Commercial grade Argon (Ar > 99.996%) with a flow rate of 14 l/min was used as shielding gas. During the deposition process, the samples were clamped on an aluminium plate at opposing sides to prevent dislocation of the sample. Further, the aluminium plate served as a heat sink, allowing an even heat dissipation during the cooling interval between layers.

In order to study the effects of different deposition patterns on the resulting material properties as well as the development of residual stress, three samples were manufactured using different deposition patterns (Fig. 3). To ensure comparability, all patterns were deposited using continuous passes of each layer without intralayer start-stop sequences. After each layer, the pattern was rotated clockwise by 90°. In addition, the deposition strategy for the spiral pattern alternated between inside/out and outside/in after each layer to avoid excess material at the center due to overlapping start-stop sequence. For the path planning of the different patterns, the *DCAM* CAD/CAM software by *SKM Informatik* was used. The total length and width of the deposit were set at 70 mm and the center-to-center distance between single deposition passes was set to 3.15 mm (Fig. 2). Each sample consists of four layers resulting in a sample height of approximately 10 mm. The samples were manufactured with identical deposition parameters using Fronius CMT + Pulse arc characteristics.

Table 2 provides a summary of the process parameters. The average current $\bar{I}_i$, voltage $\bar{U}_i$ and energy input per layer $\bar{W}_i$ were obtained from process monitoring using a *HKS WeldScanner* with a sample rate of 1 kHz. The calculation of the energy input per layer is based on Equation (1). Further, the contact tip to work piece distance was set at 15 mm.

$$W_i = \int U_i I_i dt \tag{1}$$

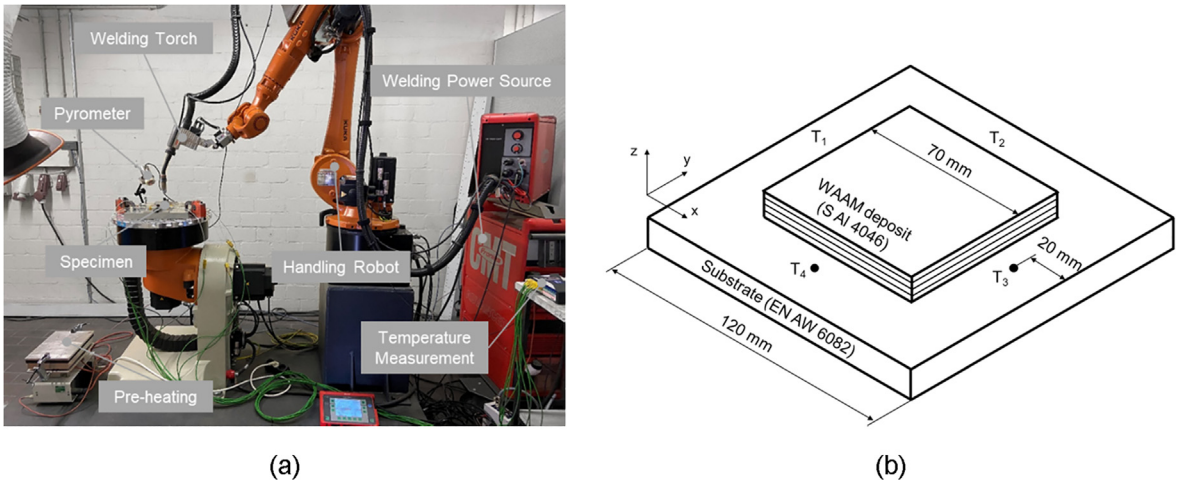

Fig. 2. Sample preparation (a) experimental setup and (b) sample geometry.

Table 1
Measured chemical composition of filler wire and nominal composition of substrate material (wt %).

Alloy	Chemical Composition (wt %)					
	Al	Mn	Mg	Si	Fe	Cu
Filler Wire: ISO 18273 - S Al 4046	bal.	<0.001	0.26	9.24	0.13	<0.001
Substrate: EN AW 6082	bal.	0.4–1.0	0.60–1.2	0.7–1.3	<0.5	<0.1

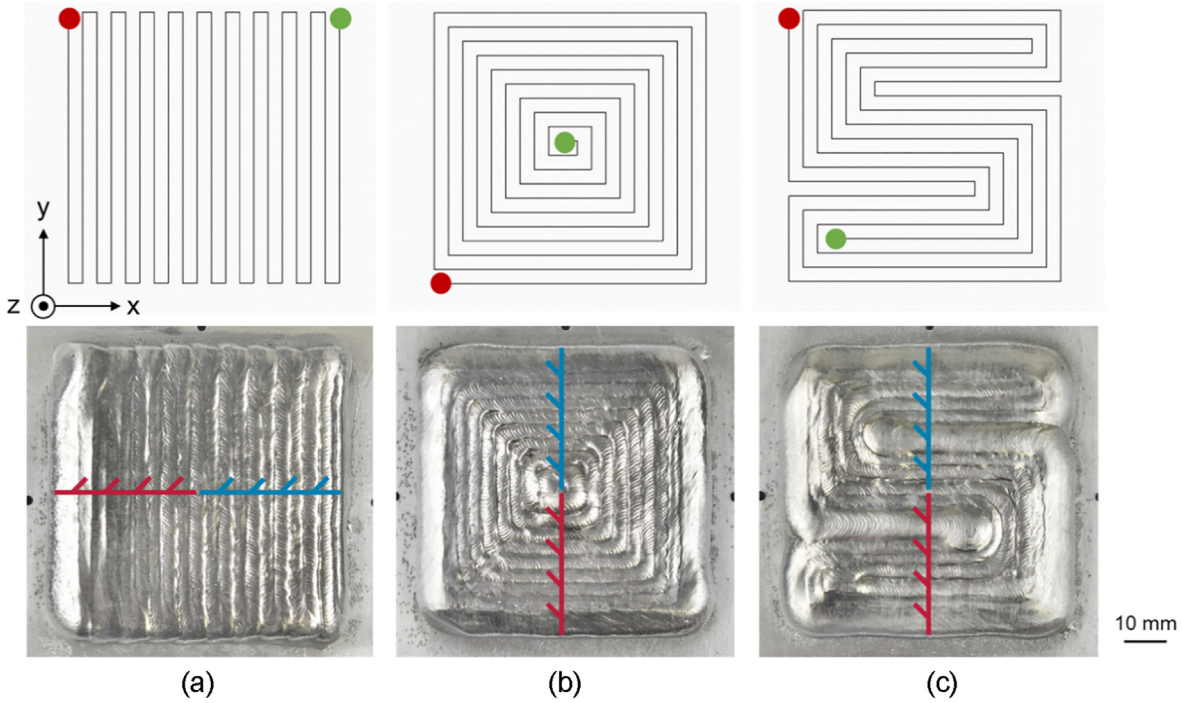

Fig. 3. Investigated deposition patterns with start (green)/stop (red) features and deposited samples; (a) meander pattern; (b) spiral pattern; (c) S pattern. Red lines point the sections of microstructural analysis; blue lines point the sections of hardness mappings. (For interpretation of the references to color in this figure legend, the reader is referred to the web version of this article.)

Preheating is beneficial for sufficient weld penetration at the start of layer sequence due to high heat dissipation. Prior to deposition, the substrate was preheated to 120 °C using a heating plate. Following sample positioning, the deposition of the first layer was started at a substrate temperature of 100 °C. After deposition of each layer, a cooling period was included by a defined intermediate time between layers. Higher interlayer temperatures can affect the geometrical uniformity due to continuous heating during the

Table 2
Process parameters for sample manufacturing.

Parameter	Value
Average Current	90.9 ± 0.3 A
Average Voltage	19.0 ± 0.7 V
Wire feed speed	6.0 m/min
Deposition speed	600 mm/min
Average energy input per layer	238.7 ± 6.9 kJ
Time between layers	t_{1-2} = 185 s t_{2-3} = 265 s t_{3-4} = 315 s

deposition process. In order to obtain comparable interlayer temperatures, the intermediate time between layers was increased after each layer according to the values given in Table 2.

2.2. Characterization methods

To determine the temperature distribution depending on the deposition pattern used, a temperature measurement was carried out using type-K thermocouples at four symmetrical arranged locations on the substrate plate. Positions for temperature measurement (T_1, T_2, T_3, T_4) are marked in Fig. 2 (b). Following the sample preparation, the samples were analyzed regarding surface residual stress, porosity, grain size and hardness.

The residual stress after the deposition process was determined by X-ray diffraction establishing the $\sin^2\psi$-method with copper-radiation source. The diffraction patterns were obtained from {333} crystalline plane of aluminum phase at 21 angles between Θ = 159° and 165°. The collimator diameter was 2 mm. For the calculation of stresses, the elastic constant ½ S_2 = 19.77 mm^2/N was chosen. Residual stress measurements were obtained along a diagonal line on top of the build-up material (Fig. 4). The specimens were not treated after deposition, except for a careful cleaning with ethanol. Hence, surface residual stress was determined in the as-deposited condition before further treatment was conducted. Stress components were determined in three directions 0°, 45° and 90° assuming plane-stress conditions. The diagonal measurement path covered almost the entire specimen width. The measurement was not conducted at the very corners of the specimen due to geometric constraints and possible measurement error resulting from rounded surfaces.

To examine the pore size and distribution as well as the total number of pores of the deposited material, X-ray computed tomography (XCT) analysis was conducted. Complete samples were scanned using a *GE phoenix vtomexs* micro XCT system with an exposure time of 600 ms, a tube voltage of 220 kV and a beam current of 160 μA. The settings resulted in a voxel (volume pixel) size of 0.1 mm. The volume reconstruction and analysis of the porosity were performed using *VGStudioMax* software. In order to solely consider valid pores and exclude measurement artifacts a threshold of 0.4 regarding the sphericity of the measured volume defects was applied. Thereby, the sphericity indicates how closely the measured defect resembles the shape of a perfect sphere (sphericity of 1.0).

Following nondestructive testing, metallographic samples used for EBSD and hardness measurement were sectioned according to Fig. 3. Metallographic samples were used for the preparation of cross-sections and hardness testing likewise. Cross-section samples were polished with up to 2 μm polishing solution and etched using Kroll etchant. Comparative hardness measurement was performed using Ultrasonic Contact Impedance (UCI) method with HV 0.5 specification. Hardness mappings of the deposited material were conducted with a line- and column-pitch of 0.4 mm. The microstructures were further characterized from outer ¼ and middle quarter length of the samples on the horizontal and plate normal centerline (Fig. 3) with ZEISS Sigma field-emission scanning electron microscope equipped with EDAX Hikari XP electron backscatter diffraction (EBSD) camera and TSL OIM software. Each material was scanned with a step-size of 2 μm for at least 4.4 mm^2 area and > 3000 identified grains with > 15° misorientation and a diameter of ≥ 3 μm, and data below a confidence index of 0.05 was excluded from the analyses before the clean-up procedure. The results of the grain size measurements are given as equivalent circle diameters.

3. Numerical procedure

In order to gain more insights into the temperature field and residual stress distribution of samples printed with different deposition patterns besides the experimental measurements, a sequential thermal–mechanical model, as shown in Fig. 5, was developed based on finite element (FE) method with ABAQUS. The material and geometry of the model match those of the printed samples. The material properties are displayed in supplementary materials. The deposition process, heat source, boundary, and substrate related parameters, as presented in Table 3, are also consistent with those of the experimental process.

In the simulation process, a moving heat source follows different patterns, and meanwhile, the elements are activated one by

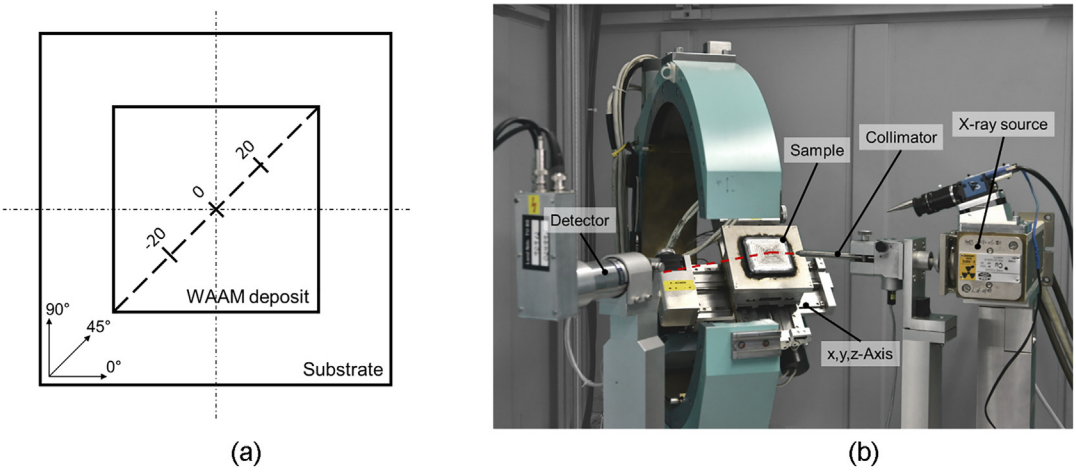

Fig. 4. Residual stress measurement (a) path and orientation for residual stress measurements; (b) XRD measurement device.

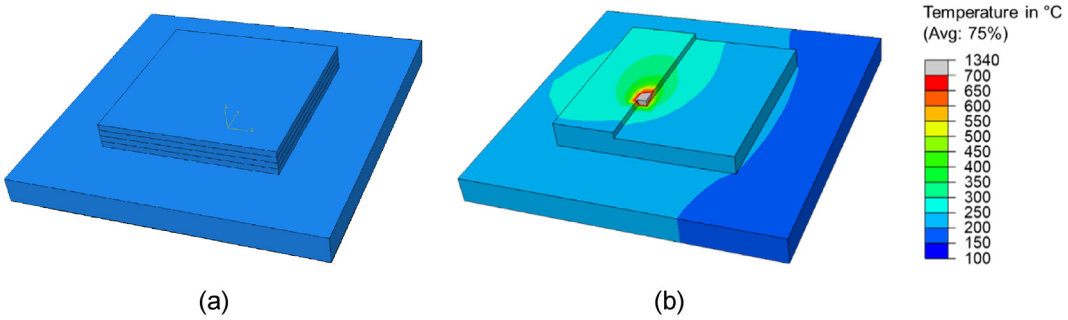

Fig. 5. FE modeling, (a) FE model geometry; (b) material adding and heat source moving process.

Table 3
Process, heat source, boundary, and substrate related parameters used in the FE analyses.

Process related parameters	Deposition layer	68 mm*68 mm*2.4 mm
	Pass width	3.4 mm
	Deposition speed	10 mm/s
	Deposition time of each layer	136 s
	Cooling time	1659 s
	Hatch angle	90°
	Initial temperature	100 ℃
Heat source related parameters	Width (b)	3.5 mm
	Depth (c)	1 mm
	Length of the front ellipsoid (a_f)	3 mm
	Length of the rear ellipsoid (a_r)	6 mm
	Fraction factor of the heat flux in the front parts (f_f)	1.2
	Fraction factors of the heat flux in the rear parts (f_r)	0.8
	Power	1729 W
Boundary related parameters	Convection heat loss	8.5 W/(m^{2}K)
	Radiation	0.8
	Ambient temperature	20 ℃
	conduction loss of the bottom surface	123 W/(m^{2}K)
Substrate related parameters	Initial temperature	100 ℃
	Geometry	120 mm*120 mm*10 mm

one (Fig. 5 (b)). The thermal analysis and mechanical analysis are performed sequentially and the temperature field as well as residual stress distribution are obtained.

In the thermal analysis, the element type used is a linear 8-node heat transfer brick (DC3D8). Thermal radiation and convection heat transfer between the active beads and the surrounding atmosphere/platform are considered. A double-ellipsoid heat source model, defined as event series data in additive manufacturing - module, is applied to the surface of a single deposition layer:

$$Q_{f/r}(x,y,z) = \frac{6\sqrt{3}Q * f_{f/r}}{a_{f/r} * b * c * \pi\sqrt{\pi}} exp\left(-\frac{3x^2}{a_{f/r}^2} - \frac{3y^2}{b^2} - \frac{3z^2}{c^2}\right) \quad (2)$$

Where the length of the front and rear ellipsoid of the heat source are represented by a_f and a_r, respectively. b is the width and c is the depth of the heat source, Q is the power input, f_f and f_r are the fraction factors of the heat flux in the front and rear parts, respectively [41]. The values of these parameters are presented in Table 3.

After the thermal analysis, the transient temperature field is applied to the subsequent mechanical analysis. The same FE mesh is used and the same process of adding material is performed while the element type is changed to the 8-node brick element with reduced integration (C3D8R). During the deposition process, the middle band of the substrate is fixed. To obtain the final residual stress of the part, the constraints are removed after the material naturally cools down to room temperature. All material properties are considered isotropic and homogenous. The softening effect of the material is - considered in this model.

4. Results

4.1. Temperature fields

During the WAAM deposition process, manufactured components experience unique thermal cycles, which dictate the microstructure and influence the mechanical properties as well as residual stress. In order to describe the thermal influences on the aforementioned characteristics depending on the deposition pattern used, temperature measurements were carried out at fixed positions on the substrate plate (Fig. 6). The temperature measurements were further used to calibrate the numerical model for residual stress calculation.

The thermal cycles from different deposition patterns are compared in Fig. 6. By example of the temperature cycle during deposition of the fourth layer (Fig. 6 (a)-(c)), particular differences in temperature distribution and peak temperature between different deposition patterns can be observed. Thereby, meander and spiral pattern show significant temperature differences between the measurement locations due to the directed movement of the deposition lanes. Further, these differences lead to an uneven temperature distribution during cooling of the sample, indicating an enhanced probability for the formation of residual stresses. It is further observed that meander and spiral pattern show comparatively higher peak temperatures at certain positions. This result can be explained by the advancing heat accumulation during the continuous deposition process in combination with the high thermal conductivity of the aluminum alloy. On the other hand, the temperature curve of the S pattern indicates a more homogeneous temperature distribution during the deposition process without prominent temperature peaks at distinct sample locations (Fig. 6 (c)). This is further emphasized by the comparison of the temperature profiles of all four layers (including cooling phases) shown in Fig. 6 (d). Based on the 90° pattern rotation after each layer, characteristic temperature profiles at the regarded measurement location can be identified particularly for meander and spiral pattern, due to the preferential direction of the deposition paths. The S pattern, however, showed no significant differences in the thermal cycles of individual layers. Furthermore, the temperature plots show differences in maximum and minimum temperatures during the processing sequences. Even though all patterns were manufactured with similar energy input as well as discrete waiting times between layers were applied, it was found that especially the meander pattern led to higher interpass temperatures.

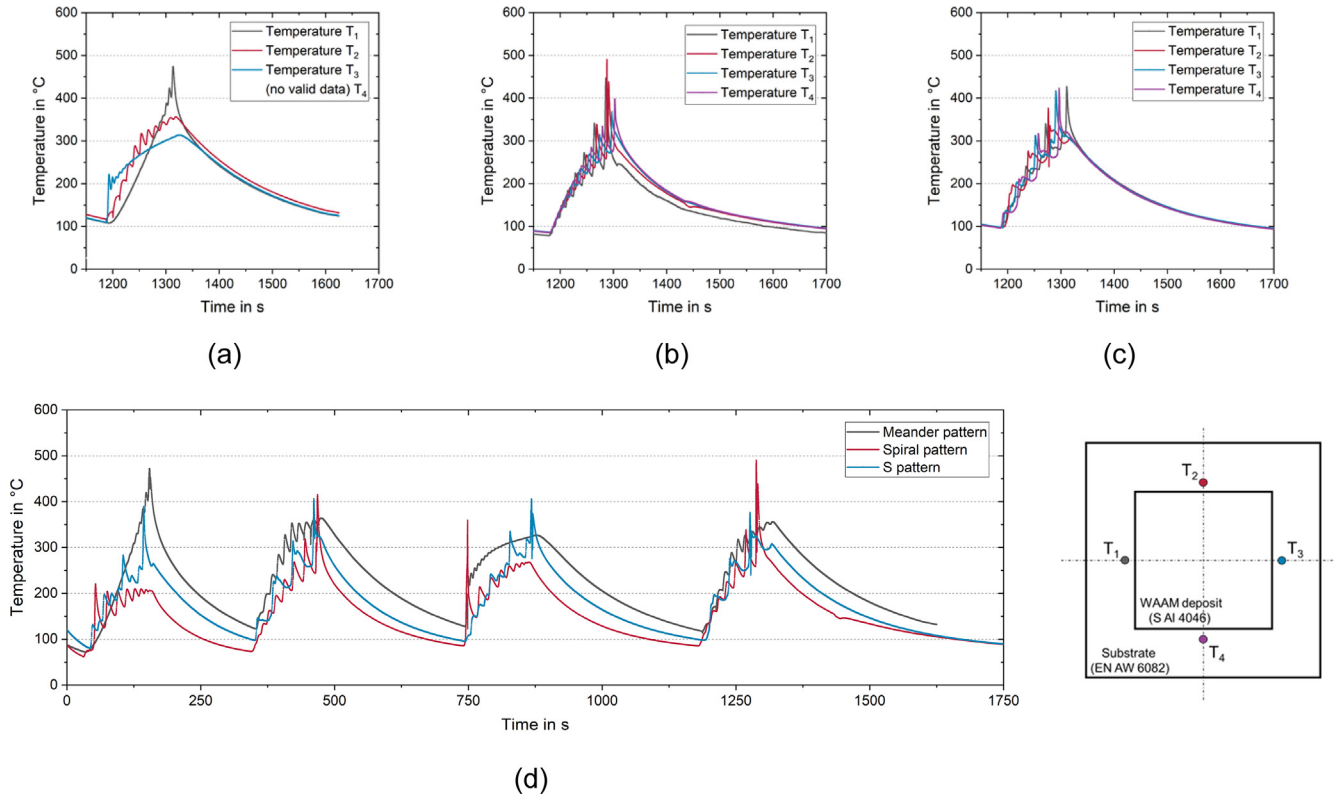

Fig. 6. Temperature distribution during the deposition of the fourth layer for (a) meander pattern, (b) spiral pattern, (c) S pattern and (d) comparison of the temperature profiles during complete deposition sequence at measurement location T_2.

In order to verify the FE thermal model, the simulated temperature history at measurement location T_2 for different patterns are compared with the experimental results in Fig. 7. As can be seen, the simulation results have a good agreement with the experimental results. The fluctuation, amplitude, and corresponding time of the simulated curves are very close to those of the experimental curves. Compared to the meander and S pattern, the spiral pattern has a larger temperature amplitude difference. A possible explanation is that due to the inherent size of the element in the FE model, there is a slight difference between the positions of T_2 in the experiment and the simulation.

The simulation results of temperature distribution at the end of the deposition process for different patterns are shown in Fig. 8. The sizes of the melting zones under the different patterns are similar and the meting temperature gradient near the melting zone is very high. Interestingly, the patterns affect the temperature distribution significantly. The spiral and S pattern generated more homogeneous temperature distributions than the meander pattern, which is consistent with the measurement results in Fig. 6.

In summary, these results suggest that both the overall temperature distribution and the peak temperature during WAAM depend on the choice of deposition pattern. Thereby, deposition patterns with preferential directions of the deposition path, such as meander and spiral pattern, can lead to uneven temperature fields or high local peak temperatures.

4.2. Porosity

Fig. 9 (a-c) provides the scan images of XCT analysis, with the volume of inner defects depicted in pseudo color. As shown in the images, the deposited materials contain a significant number of finely dispersed individual pores. Fig. 9 (d-f) presents the peak temperature of the deposition beads on the top layer calculated by the FEM model. It can be seen that comparatively large pores occurred predominantly in regions of temperature peaks and arc start/stop-features within the patterns. This applies specifically to the outer edges of meander and spiral pattern as well as the diagonal and center region of spiral pattern. Further, XCT analysis revealed the appearance of isolated lack of fusion defects in the first deposition layer for spiral and S pattern. These defects solely occurred in regions with 90° turning points of the deposition path. No further lack of fusion defects appeared in subsequent layers.

The porosity is further quantified by the scatter plot depicted in Fig. 9 (h). Due to the large number of finely dispersed individual pores, the median pore volume shows comparable values of 0.03 mm^3 for meander pattern and 0.02 mm^3 for spiral and S pattern. However, the cumulative pore volume contained in the deposited volume showed values of 768 mm^3 for meander pattern, 556 mm^3 for spiral pattern and 420 mm^3 for S pattern, indicating a higher amount of particularly large pores using meander and spiral pattern. In relation to the build-up volume, measured pore volumes ranged from approx. 0.9 % for S pattern and 1.6 % for meander pattern respectively. As shown in Fig. 9 (g), the sphericity of measured defects exhibits a peak at approx. 0.9 for all three patterns, suggesting that the detected defects predominantly consist of gas porosity. It is further visible that the spiral pattern contains a slightly higher count of low sphericity defects. This can be attributed to the lack of fusion defects observed during visual inspection.

4.3. Metallurgical and mechanical properties

Macroscopic cross-sections and the corresponding results of UCI hardness mappings in the as-deposited condition are summarized in Fig. 10. Hardness values in the as-deposited material range from approx. 50 to 90 $HV_{0.5}$ with the top layers having higher hardness compared to the remaining material, indicating annealing-

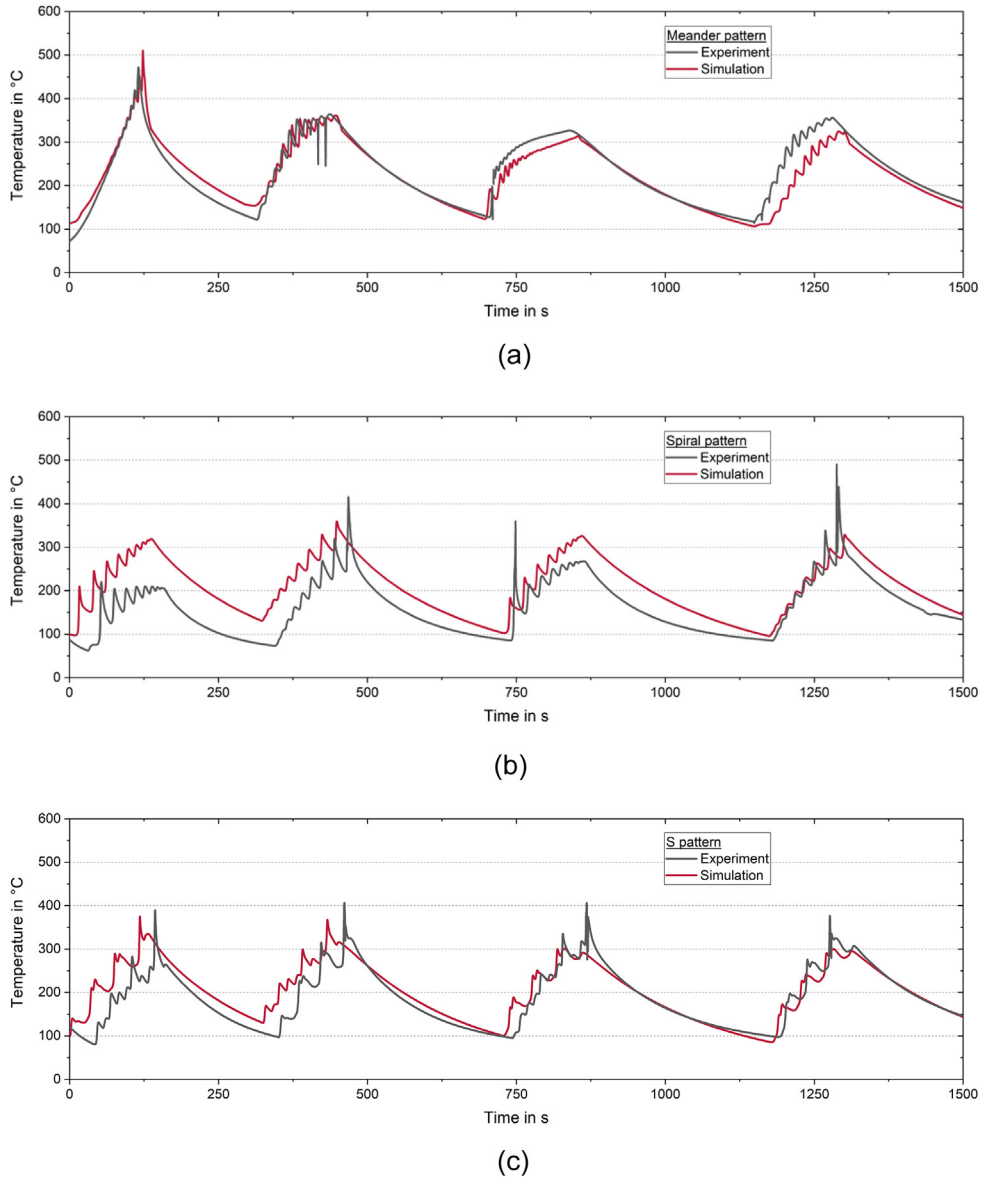

Fig. 7. Comparison of simulation and experimental results of temperature history at measurement location T_2 during the deposition of the four layers for (a) meander pattern, (b) spiral pattern, (c) S pattern.

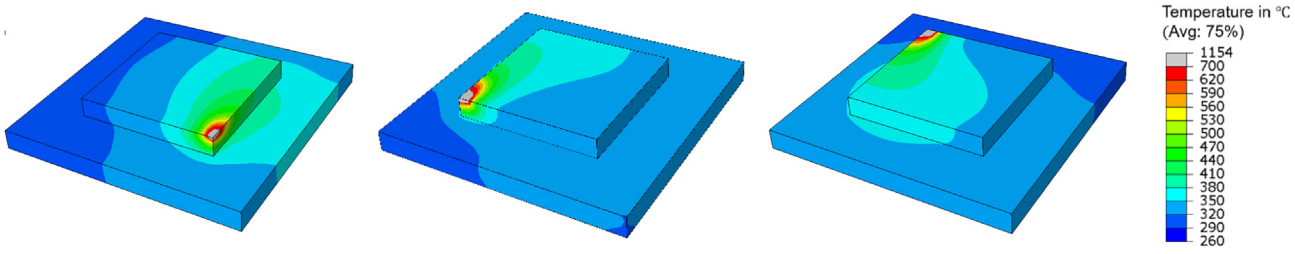

Fig. 8. Simulation results of temperature distribution at the end of deposition process for (a) meander pattern, (b) spiral pattern, (c) S pattern. The grey color area indicates the melting zone.

caused softening by periodic reheating of the structure and a resulting change in precipitation size. Furthermore, reduced hardness values appear along the fusion lines of single deposition passes regardless of the used deposition pattern. This is due to coarse-grain zones, as shown in microstructural analysis (Fig. 12).

The microstructures are similar in all three patterns with heterogeneous grain size distribution typical of welds. Larger aluminum grains consist of several cells, and the cell surfaces are populated by Si-eutectoid precipitates (Fig. 11) [42]. Fig. 11 shows NTS BSD backscatter images of S pattern: (a)

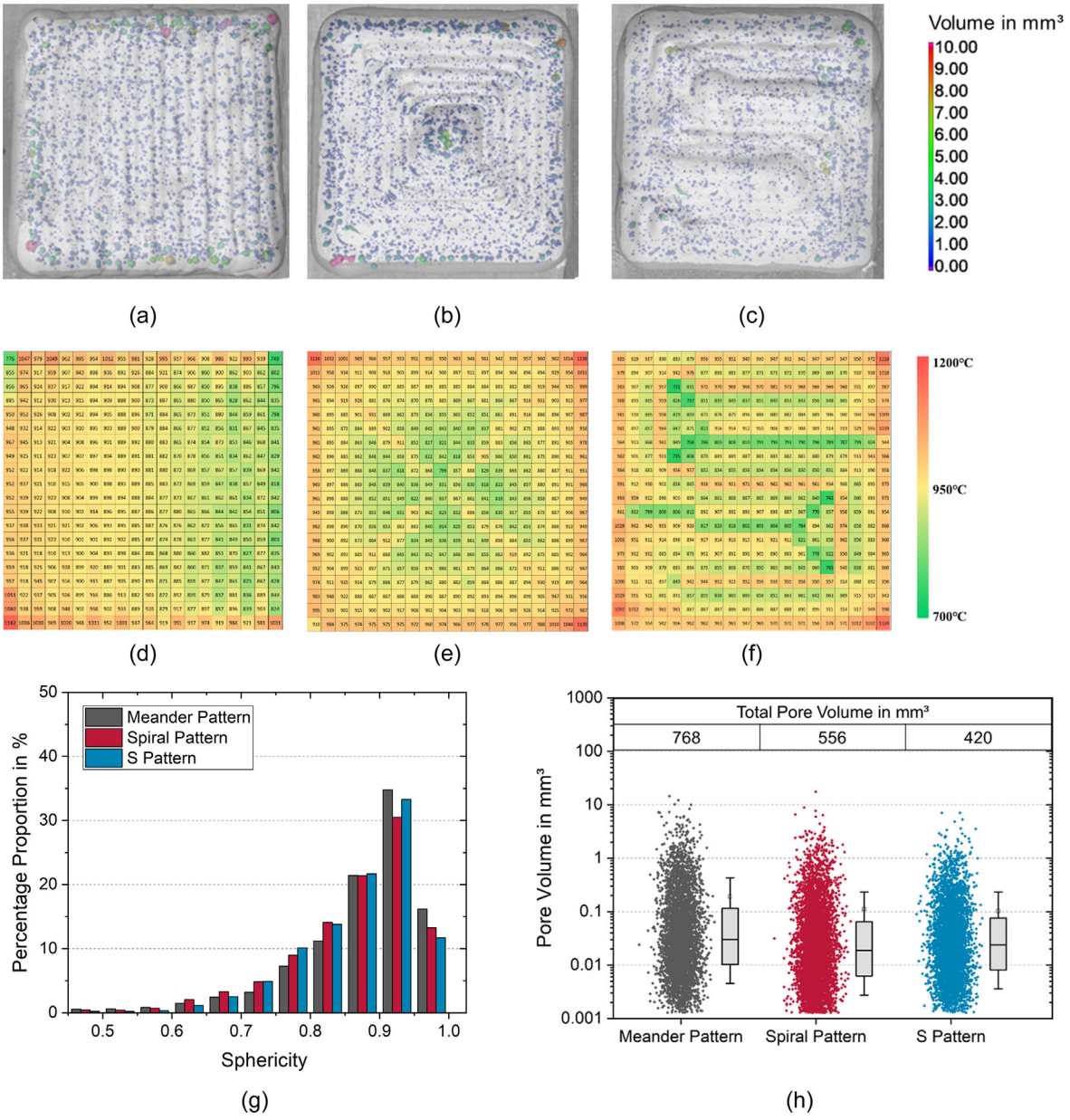

Fig. 9. XCT images of (a) meander pattern, (b) spiral pattern, (c) S pattern and peak temperature of the deposition bead on top layer of (d) meander pattern, (e) spiral pattern, (f) S pattern and (g) the effect of different deposition patterns on pore sphericity and (h) the distribution of pore volume.

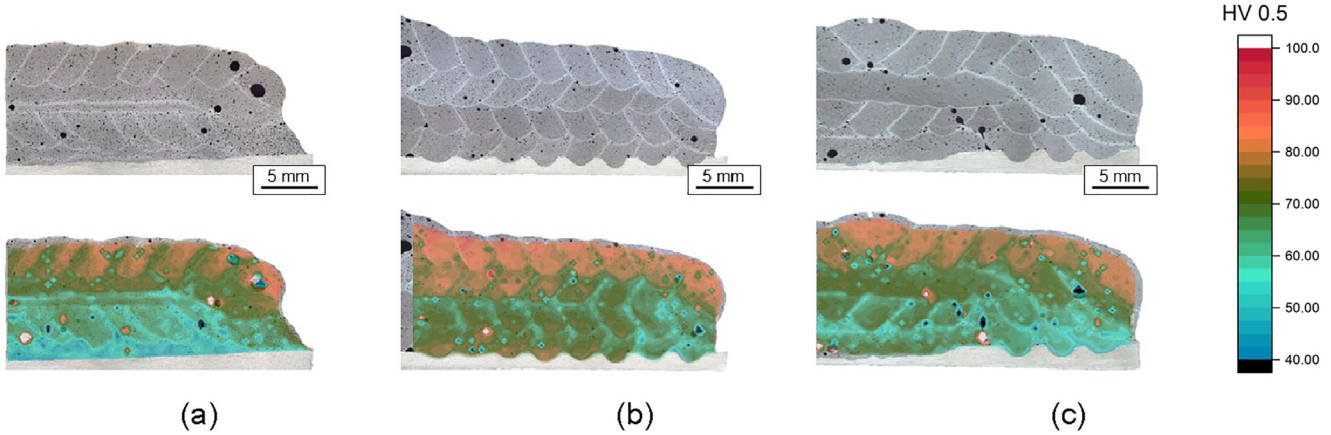

Fig. 10. Cross-section samples and corresponding UCI hardness mappings of (a) meander pattern, (b) spiral pattern and (c) S pattern.

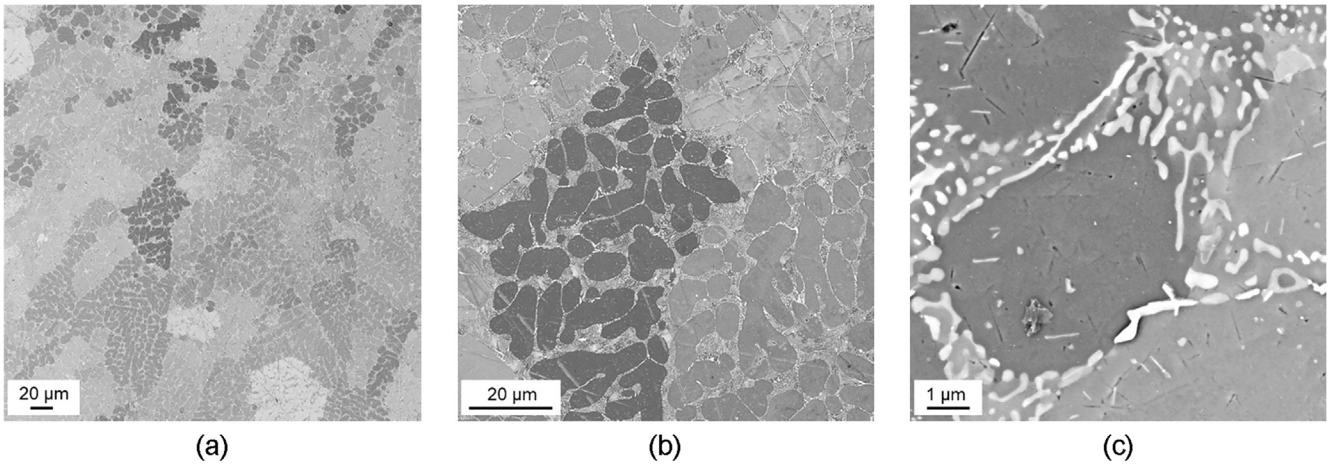

Fig. 11. NTS BSD (backscatter) detector images of the S pattern microstructure: a) grain structure, b) cell structure, c) Si-eutectoid precipitates.

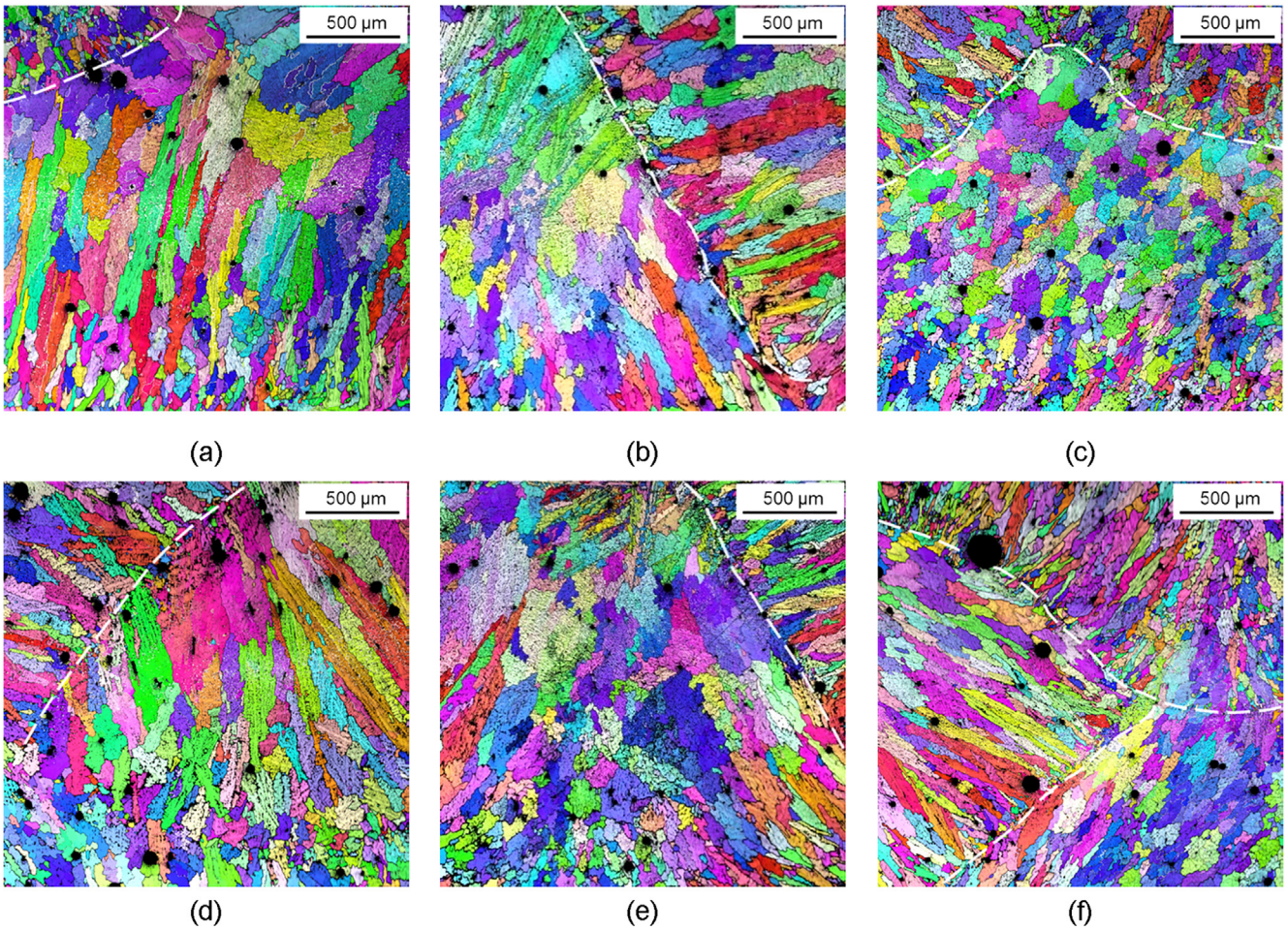

Fig. 12. Mixed image quality + inverse pole figure images of the microstructures: Meander (a) and (d), Spiral (b) and (e), and S pattern (c) and (f). (a) - (c) show the microstructure on the middle of 2nd quarter length, and (d) – (f) on the 1st quarter length closer to deposited edges. Fusion lines are marked with dashed white lines. Boundaries with > 15° misorientation are highlighted with black lines, and boundaries 5 – 15° with white lines.

highlighting the grains reflecting their orientational differences on the polished surfaces, (b) visualizing the cell structures varying in size and shape in the grains middle of (a), and (c) showing the mostly rod-like Si-eutectoid precipitates bordering the Al-cells as brighter areas due to their higher atomic radius. An apparent difference between the patterns is the higher qualitative fraction of Si-eutectoid precipitates in spiral pattern than the other two (not shown here) due to higher peak temperatures (Fig. 6). The different shades of the aluminum grains in Fig. 11 are expected to arise from their different orientations rather than from grain-level segregation of the alloying elements.

Both meander pattern (Fig. 12 a) and spiral pattern (Fig. 12 b) possess very large elongated grains in the coarse-grain zones below the bead interfaces, but S pattern can show also pronounced equiaxed grain morphologies with suppressed grain growth (Fig. 12 c). This is due to evenly varying deposition direction in all the x-y directions, also as compared to similarly varying meander pattern (Fig. 10). Grain analysis shows that while the average grain sizes are close to each other, both the effective coarse grain size at the 80% of cumulative distributions ($d_{80\%}$) [43] and the relative grain size dispersion [44] are clearly the smallest for S pattern (Table 4, Fig. 13 a). This same trend persists also with analysis considering misorientations > 5° (Table 4). The effect of higher maximum temperatures with the spiral pattern causes pronounced dendritic growth (Fig. 12 (b) and (e)) not observed in meander nor S pattern. Fig. 13 (b) emphasizes the lower amount of very large grains in S pattern and the bimodal grain size distribution for all the patterns.

4.4. Residual stress distributions

Residual stress was analyzed in a two-staged approach depending on the deposition patterns. At first, the surface residual stress was determined by means of XRD as described in Section 2. Due to the limited meaning of surface residual stress alone, an in-depth analysis was performed with help of FE models in a second stage. The surface residual stress from experiments and numerical models are compared and used for verification purposes. The verified FE models are used to study different stress components, residual stress gradients and global residual stress maxima.

The experimentally determined residual stress distributions are shown in Fig. 14. The results show relatively homogeneous residual stress distributions along the measurement paths for all three deposition patterns. Residual stress components (0°, 45°, 90°) show similar magnitudes and trends within each pattern. The estimated mean values of residual stress magnitudes at the surface ranges between −20 MPa (a) and 0 MPa ((b) and (c)). Furthermore, all three patterns reveal some specific local residual stress features near locations of the start and stop of deposition passes. Locations of local tensile residual stress peaks correlate with deposition stop locations (pattern (a) and (c)) and final deposition beads (b). The scatter from measurement is in the order of ± 10 MPa to ± 20 MPa, results from the linear fit of the $\sin^2\Psi$-method, and is mainly related with coarse grain weld metal.

The simulation and experimental results of residual stresses along the diagonal direction of the top surface of the deposition part for the S pattern are compared in Fig. 15. For both the equivalent residual stress (σ_e) and maximum principal residual stress (σ_1), as well as residual stress components (σ_{11} and σ_{22}), the simulated curves are close to the experimental curves. Next to the measurement error, the other source of inaccuracy is the lack of representative temperature-dependent material properties. However, the overall simulation and experiment results are in good agreement.

The residual stress fields under all three patterns are also analyzed. Table 5 summarizes the σ_1 distribution of the three analyzed patterns in different views. The σ_1 field of the whole part under three patterns are displayed in sub-figures (a-c). Compared to the spiral and S pattern, the meander pattern generated higher residual stress. It is mainly because the temperature distribution of the meander pattern is less homogenous. Another interesting finding is that the residual stress near the interface between the deposition layer and the substrate is relatively high owing to the mismatch of material properties between the substrate and the deposited part and low degree of freedom of the interface. Residual stress is known to be released through material deformation. Since the degree of freedom of the interface is low, more stress is concen-

Table 4
The grain size analysis: average grain size (d_{avg}), effective coarse-grain size $d_{80\%}$, and grain-size dispersion Δ for both grains over > 15° and > 5° misorientations.

	>15°				>5°		
	$d_{avg.}$ (μm)	$d_{80\%}$ (μm)	Δ ($d_{99\%}$-$d_{1\%}$)/$d_{avg.}$	Number	$d_{80\%}$ (μm)	Δ ($d_{99\%}$-$d_{1\%}$)/$d_{avg.}$	Number
Meander	26	221	18.7	3171	180	22.0	5248
Spiral	34	233	19.3	3699	161	25.6	6603
S	27	143	14.9	3612	115	11.0	5560

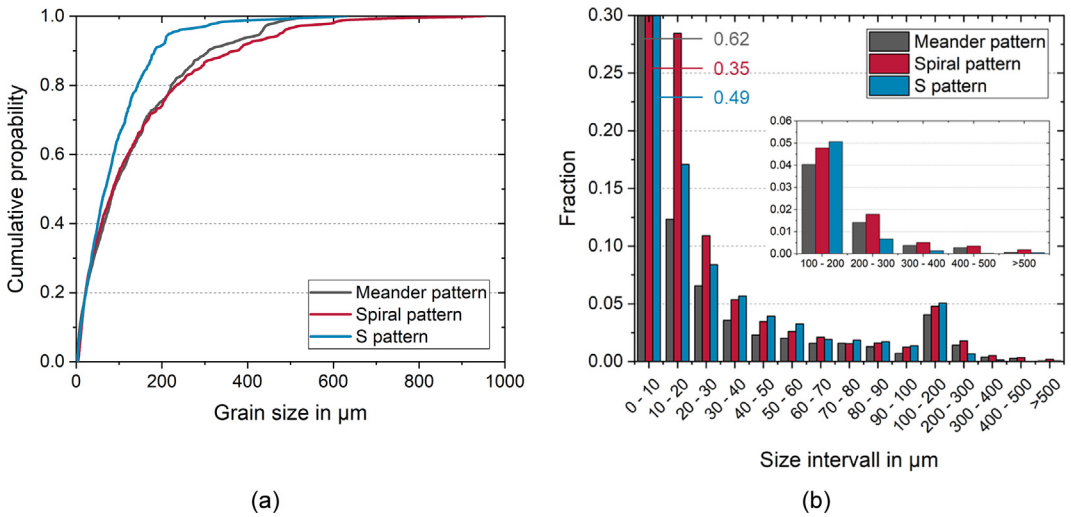

Fig. 13. (a) cumulative probabilities for the grain size distributions emphasizing the clearly smaller coarse grains with the S pattern; (b) fractions per size intervals below and above 100 μm.

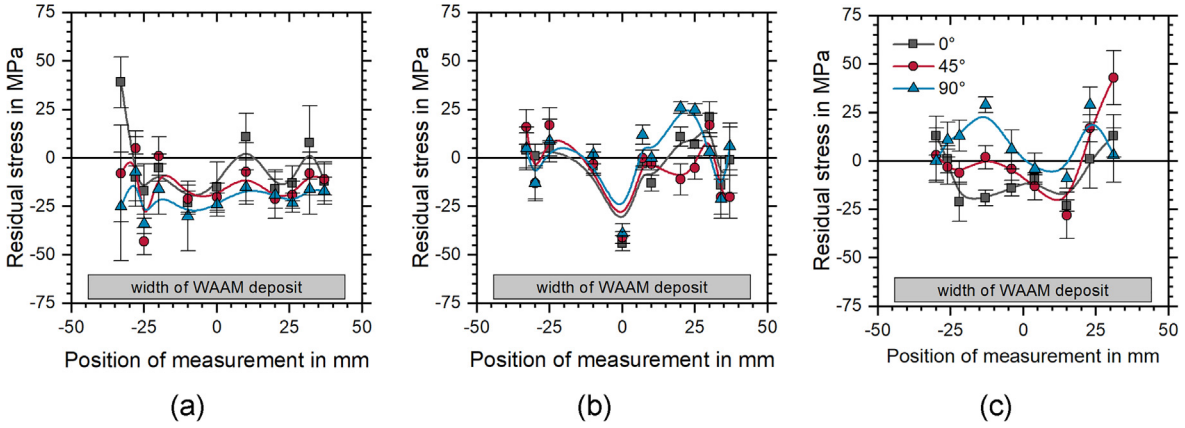

Fig. 14. Residual stress on sample surface for (a) meander pattern, (b) spiral pattern, (c) S pattern; measurement locations are depicted in Fig. 4.

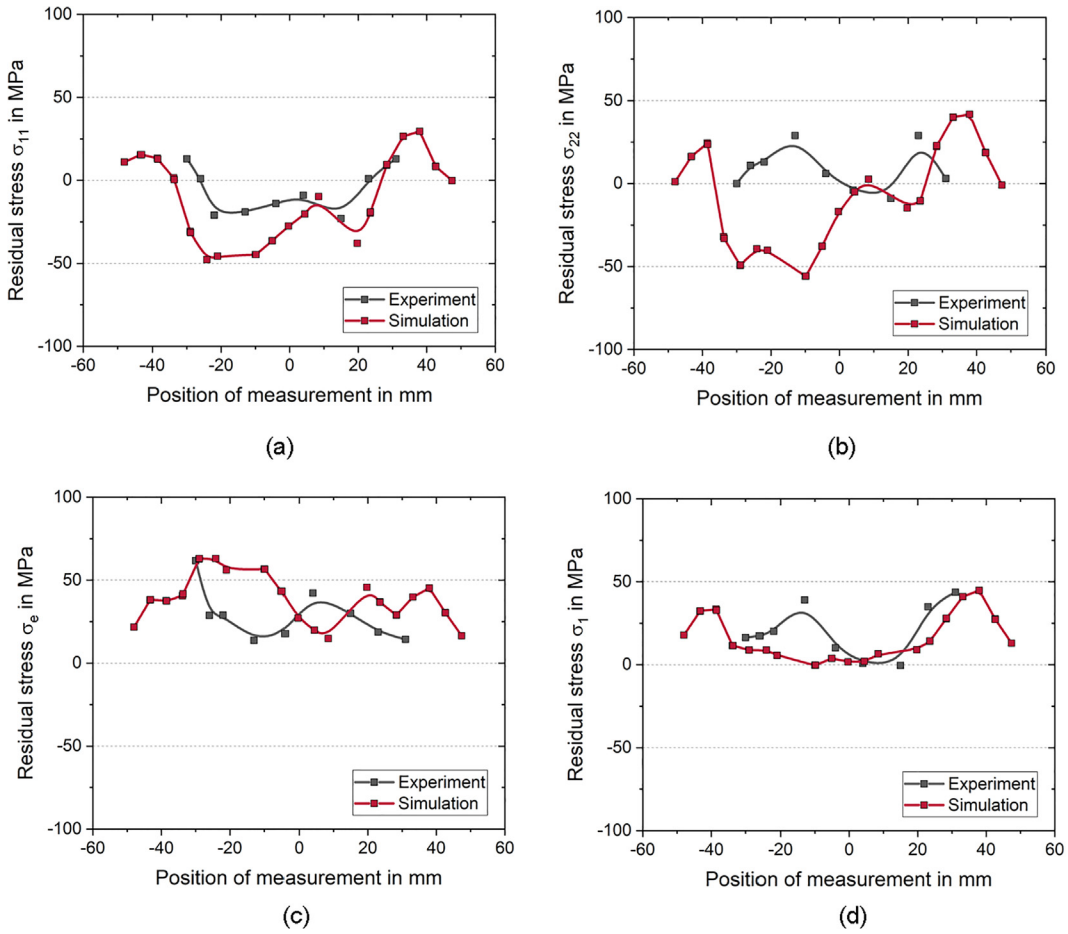

Fig. 15. Comparison of simulation and experimental results of residual stresses for S pattern (a) σ_{11}, (b) σ_{22}, (c) σ_e and (d) σ_1; Experimental data determined from mean values shown in Fig. 14.

trated at the interface. The σ_1 fields of the half cross-section under these three patterns are presented in sub-figures (d-f). As can be seen, the residual stress near the interface is higher and non-continuous and the S pattern generated the most uniform residual stress distribution.

The effect of the deposition pattern on the residual stress is further explored by analyzing the residual stress distribution of various positions. The σ_1 fields at the top surface of the parts under the three deposition patterns are presented in sub-figures (g-i). Compared with the corresponding deposition pattern of the top layer (Fig. 2), the residual stress at the end of the deposition pattern of the top layer is higher because of higher peak temperature due to heat accumulation during the deposition process and higher cooling rates. For example, the residual stress on the left side for the meander pattern is higher than that on the right side (sub-figure (g)), as the material of the top layer is deposited from right side to left side. In general, the spiral and S pattern generate more uniform residual stress distributions than the meander pattern

Table 5
σ_1 distribution of whole part (a, b, c), cross-section of half part (d, e, f), and top (g, h, i) and bottom (j, k, l) surfaces of deposition part under three patterns.

	Meander	Spiral	S
Whole	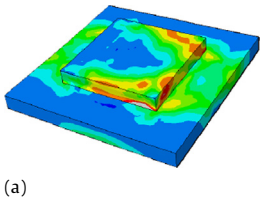 (a)	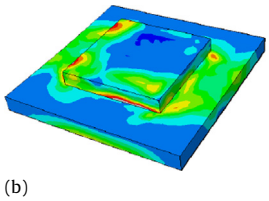 (b)	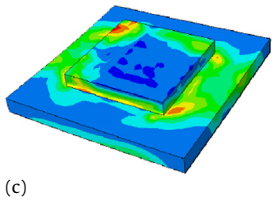 (c)
Cross-section	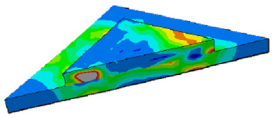 (d)	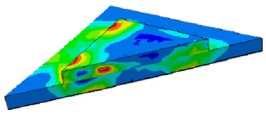 (e)	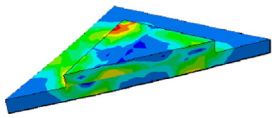 (f)
Top surface	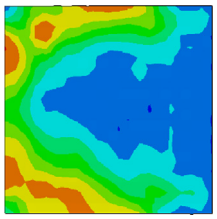 (g)	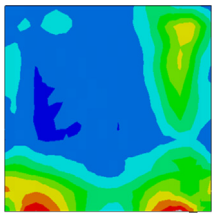 (h)	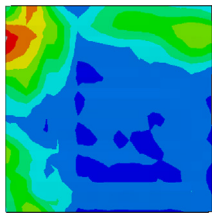 (i)
Bottom surface	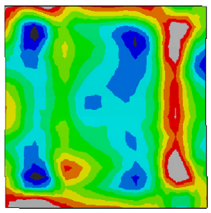 (j)	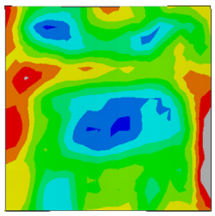 (k)	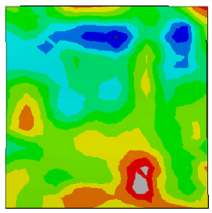 (l)

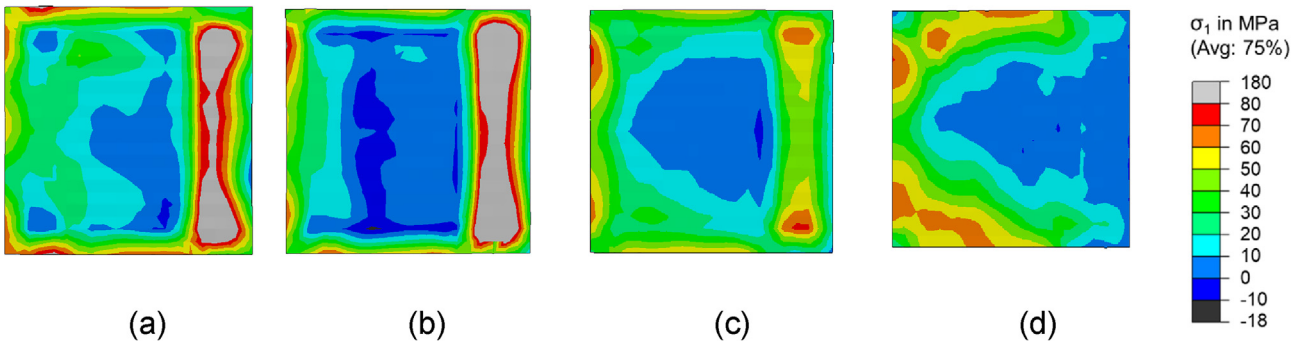

Fig. 16. σ_1 distribution of different layers under meander patterns at the (a) first layer, (b) second layer, (c) third layer, (d) fourth layer.

because the temperature distribution of spiral and S patterns are more homogeneous compared to the meander pattern, as discussed in section 4.1. The σ_1 distribution at the bottom surface is opposite to that of the top layer to a certain extent. The top layer exhibits predominantly compression, while the bottom surface is mostly tensile. This is stemming from the bending of the substrate after releasing the clamping.

To further analyze the distribution characteristics of residual stress inside the deposition parts, the σ_1 distributions of four layers under meander pattern are presented in Fig. 16. In general, the middle part of each layer has lower residual stress than the edge part. In contrast to the fourth layer (top layer), the residual stress distribution of the first three layers is independent of their deposition pattern. The reasons are that the residual stress is redistributed during the deposition process of upper layers and the printing orientation of each layer is rotated by 90°. Comparing to the third and fourth layers, the first and second layers have higher residual stresses as the degree of freedom of the material is lower close to the fixed substrate. Furthermore, the residual stress of the top layer is larger than that of the third layer. This is because the fourth layer reheats the third layer and the residual stress is redistributed and released to some extent.

The maximum residual stress is critical for the performances of printed components because the areas with the highest residual stress are usually the parts of the component with the weakest strength. Hence, it is also an important indicator for evaluating the deposition patterns. The simulation results of the maximum residual stresses of the deposited part printed by different patterns are summarized in Fig. 17. The maximum residual stresses (σ_e, σ_1, σ_{11} and σ_{22}) of spiral and S pattern are very close to each other and

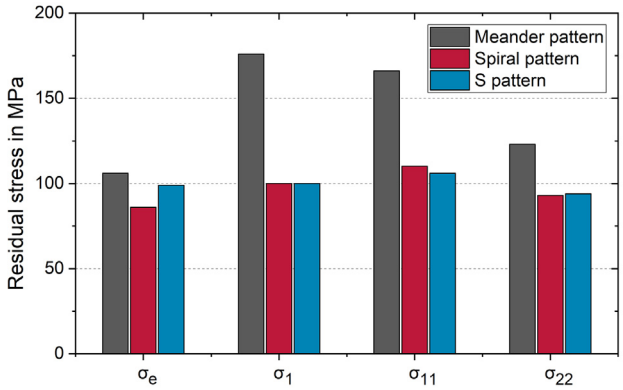

Fig. 17. Summary of maximum residual stresses of deposition part for different patterns.

much lower than those of meander pattern. This stems from the fact that spiral and S pattern achieve more uniform temperature distribution, which has been discussed in depth in [40]. Regarding the residual stress, it can be concluded that residual stress distribution is highly dependent on the uniformity of the temperature distribution, and S and spiral pattern are more promising than meander pattern.

In summary, there are many factors influencing the residual stress distribution, such as the degree of freedom, boundary condition, material properties, cooling rate, and uniformity of temperature distribution. The deposition pattern has a significant effect on residual stress distribution since it determines the temperature field. A more uniform temperature distribution will produce lower residual stress. In this work, the spiral and S pattern generated lower residual stress than the meander pattern, and the S pattern produces the most uniform residual stress distribution. In addition to comparing the resulting residual stresses under three patterns, an analysis of some general distribution characteristics of the residual stress of deposition parts is performed. It is found that the center part and the top surface of the deposited parts have lower residual stress than the edge part and the bottom surface, respectively. This is because the substrate bends upward after the constraint is released, which in turn causes these positions to be compressed. Another finding is that due to the higher cooling rate, the residual stress near the end of the deposition pattern of the top layer is higher. In addition, the residual stress is higher at the interface between the substrate and the built part due to the lower degree of freedom and mismatch of the materials.

5. Discussion

Evaluating the results obtained using different deposition patterns, visual inspection showed distinct differences in the surface accuracy of the finished samples. Thereby, the meander pattern resulted in a more even surface. Compared to meander pattern, spiral pattern showed excess material located at the center of the spiral and S pattern resulted in a noticeable waviness of the surface. The comparatively uneven surface appearance using the S pattern is related to the inflection points of the deposition paths allocated across the deposit. Furthermore, prior studies have noted that arc start/stop-positions often result in slightly deviating deposition geometries. These deviations accumulate with increasing number of layers. In case of the spiral pattern, the arc start/stop-positions are always located at the center of deposition, regardless of the pattern rotation, resulting in a comparatively high deviation.

According to both the experimental and the numerical results, the choice of deposition pattern affects particularly the temperature distribution during deposition and thus the resulting material properties. In this study, the S pattern provided a more homogeneous temperature distribution with lower peak temperatures compared to meander and spiral pattern. This may be explained by the multidirectional deposition path during manufacturing, which prevents heat accumulations at certain locations. In contrast, the directional deposition paths of meander and spiral pattern are leading to a constant increase in temperature in deposition direction, evoking an enlargement of the molten pool. The differences in temperature distribution can further be related to the resulting material properties. In terms of porosity formation, the results indicate the formation of increased pore volume in areas related to higher process temperatures. Accordingly, the S pattern showed a comparatively lower overall pore volume due to lower temperature peaks. Furthermore, increased porosity was observed at arc start/stop-positions. However, it is common for WAAM components to undergo post processing. If the arc start/stop-positions are located at the outer edges of components, locations of increased porosity are likely to be removed during final machining of the components. In this case, it is beneficial to move arc start/stop-positions to the outer contour. Regardless of the deposition pattern, a heterogeneous microstructure with elongated coarse grains near the fusion lines and fine grains in the interlayer regions were detected. The microstructures for all three patterns are similar to what has been reported for Al-Si alloy castings [42,45] and thus differ from dendrite-dominated WAAM with higher arc energy [45]. The average grain size falls slightly larger than those of selected laser melting produced AlSi10Mg (<20 μm) and WAAM alloy 4047 [45,46], but are approximately same size or smaller than for 4047-casts [45] and electron beam melted AlSi10Mg [47], respectively, although direct comparison is limited due to varying sampling parameters. Within the patterns studied here, beneficial smaller effective coarse grain size and size dispersion of S pattern promise improved mechanical properties over the other two patterns [43,44]. These results can be attributed to the more homogeneous temperature distribution and therefore lower temperature gradients during solidification. However, hardness measurements showed a significant softening of the bulk material in all samples due to the thermal conditions during deposition. A final heat treatment of the component is therefore recommended and should be topic of further studies. Residual stress formation is generally dependent on the cooling conditions and aided by temperature differences during the cooling of the structure. Accordingly, surface residual stress measurements as well as the calculations from the mechanical model revealed local residual stress features in regions of arc start/stop-positions due to local temperature concentrations. Attributed to the high heat conductivity of aluminum, surface residual stress measurements showed overall comparable results for each pattern, with values in the same order of magnitude as described in [24] for WAAM deposited 4043-grade aluminum. However, the simulation results could further analyze the distribution characteristics of residual stress inside the deposited parts. The results of global residual stress maxima suggest that the spiral and S pattern can reduce stress concentration. The simulated residual stress field identifies the local tensile stress concentrations at the interface of substrate, the first two layers and the edge part of the deposited part. These findings indicate that residual stress distribution has a close correlation with the deposition patterns, material, geometry of substrate and boundary condition.

The findings of this study provide an in-depth understanding on how the part quality and residual stress formation during WAAM of aluminum is affected by the applied deposition pattern and temperature distribution, respectively. In large parts, the recently developed S pattern provided beneficial results compared to conventional meander and spiral pattern in terms of material proper-

ties. As mentioned in the introduction, the WAAM process is particularly suitable for the production of complex shaped components. Accordingly, building on these promising results, further work should include the establishment of a method for applying the S pattern to nonlinear geometries, as well as studies on geometric accuracy. In addition, the residual stress development with increasing number of layers should be scope of further research.

6. Conclusions

The present research examined the influence of three deposition patterns used in WAAM on the properties of the deposited material. The samples were analyzed regarding temperature profiles, internal irregularities, microstructure and surface residual stress distribution. Sequential thermal–mechanical models for further evaluation of the temperature profiles during manufacturing process and residual stress distributions in the manufactured samples were created. The following key aspects could be derived from this study:

- The temperature distribution during the processing sequence is strongly dependent on the used deposition pattern, affecting the homogeneity of the temperature distribution as well as local peak temperatures. Both the temperature field and the cooling rates were found to determine the deposition quality in terms of internal irregularities (pores, lack of fusion), microstructure and residual stress formation.
- XCT analysis revealed increased porosity in areas with high peak temperatures (edge area of the deposit) and high temperature gradients (arc start/stop-features). Further, deposition patterns with rectangular deposition paths showed isolated lack of fusion defects in corner areas.
- The microstructures resulting from the different patterns are similar to each other with Al grains with size distributions typical to weld metal obtained during conventional GMAW, and sub-grain cell structure with Si-eutectoid precipitates around the Al cells. However, due to differences in the cooling paths, the size of the coarsest grains and grain size dispersion are effectively suppressed with the S pattern. Hardness mappings indicate significant softening of the material due to the temperature effects of subsequent layers. Accordingly, post-weld heat treatment is recommended and should be a scope of further research.
- Measured surface residual stress showed comparable magnitudes and trends within the different deposition patterns. Specific residual stress differences could be detected in areas of arc start/stop-features, resulting in local tensile residual stress peaks.
- The simulation results confirmed the occurrence of higher residual stress at the end of the deposition pattern. Further, a peak in tensile residual stress was determined near the interface between the deposition layer and the substrate depending on the clamping during the deposition process.
- The direct comparison of the patterns examined in this study shows that S pattern can lead to reduced porosity, low residual stress as well as comparatively smaller coarse grain size, due to a more homogeneous temperature distribution.

CRediT authorship contribution statement

Markus Köhler: Conceptualization, Formal analysis, Investigation, Writing – original draft, Visualization. **Li Sun:** Conceptualization, Methodology, Software, Formal analysis, Writing – original draft, Visualization. **Jonas Hensel:** Conceptualization, Methodology, Validation, Formal analysis, Investigation, Writing – original draft, Writing – review & editing, Visualization, Project administration. **Sakari Pallaspuro:** Conceptualization, Formal analysis, Investigation, Writing – original draft, Writing – review & editing, Visualization. **Jukka Kömi:** Resources, Supervision, Funding acquisition. **Klaus Dilger:** Resources, Supervision. **Zhiliang Zhang:** Conceptualization, Validation, Resources, Writing – review & editing, Supervision, Project administration, Funding acquisition.

Declaration of Competing Interest

The authors declare that they have no known competing financial interests or personal relationships that could have appeared to influence the work reported in this paper.

Acknowledgments

Dr. Li Sun would like to thank the founding from the China Scholarship Council and the Research Council of Norway through the Petromaks2 program (Project No. 281927) and the BIA Program (Project No. 269558)). Dr. Sakari Pallaspuro would like to thank Academy of Finland (#311934) for funding.

Appendix A. Supplementary material

Supplementary data to this article can be found online at https://doi.org/10.1016/j.matdes.2021.110122.

References

[1] Z. Pan, D. Ding, B. Wu, D. Cuiuri, H. Li, J. Norrish, Arc Welding Processes for Additive Manufacturing: A Review, in: S. Chen, Y. Zhang, Z. Feng (Eds.), Transactions on Intelligent Welding Manufacturing, Transactions on Intelligent Welding Manufacturing, Springer Singapore, Singapore, 2018, pp. 3–24.
[2] K.S. Derekar, A review of wire arc additive manufacturing and advances in wire arc additive manufacturing of aluminium, Materials Science and Technology 34 (8) (2018) 895–916, https://doi.org/10.1080/02670836.2018.1455012.
[3] D. Ding, Z. Pan, D. Cuiuri, H. Li, Wire-feed additive manufacturing of metal components: Technologies, developments and future interests, Int J Adv Manuf Technol 81 (1–4) (2015) 465–481, https://doi.org/10.1007/s00170-015-7077-3.
[4] J. Liu, Y. Xu, Y. Ge, Z. Hou, S. Chen, Wire and arc additive manufacturing of metal components: a review of recent research developments, Int J Adv Manuf Technol 111 (1–2) (2020) 149–198, https://doi.org/10.1007/s00170-020-05966-8.
[5] J. Xiong, Z. Yin, W. Zhang, Closed-loop control of variable layer width for thin-walled parts in wire and arc additive manufacturing, Journal of Materials Processing Technology 233 (2016) 100–106, https://doi.org/10.1016/j.jmatprotec.2016.02.021.
[6] J. Bai, H.L. Ding, J.L. Gu, X.S. Wang, H. Qiu, Porosity evolution in additively manufactured aluminium alloy during high temperature exposure, IOP Conf. Ser.: Mater. Sci. Eng. 167 (2017) 12045, https://doi.org/10.1088/1757-899X/167/1/012045.
[7] M. Köhler, S. Fiebig, J. Hensel, K. Dilger, Wire and Arc Additive Manufacturing of Aluminum Components, Metals 9 (5) (2019) 608, https://doi.org/10.3390/met9050608.
[8] V. Balasubramanian, V. Ravisankar, G. Madhusudhan Reddy, Effect of pulsed current welding on mechanical properties of high strength aluminum alloy, Int J Adv Manuf Technol 36 (3–4) (2008) 254–262, https://doi.org/10.1007/s00170-006-0848-0.
[9] J.R. Hönnige, P.A. Colegrove, S. Ganguly, E. Eimer, S. Kabra, S. Williams, Control of residual stress and distortion in aluminium wire + arc additive manufacture with rolling, Additive Manufacturing 22 (2018) 775–783.
[10] M. Workowski, T. Nitschke-Pagel, K. Dilger, Load induced inhomogeneous plastic deformations in welded aluminium joints, Weld World 58 (4) (2014) 529–538, https://doi.org/10.1007/s40194-014-0136-9.
[11] F. Teichmann, A. Ziemer, M. Leitner, J. Hensel, K. Dilger, Linear Elastic FE-Analysis of Porous, Laser Welded, Heat Treatable, Aluminium High Pressure Die Castings Based on X-Ray Computed Tomography Data, Materials 13 (6) (2020) 1420, https://doi.org/10.3390/ma13061420.
[12] P. Yousefian, M. Tiryakioğlu, Pore Formation During Solidification of Aluminum: Reconciliation of Experimental Observations, Modeling Assumptions, and Classical Nucleation Theory, Metall and Mat Trans A 49 (2) (2018) 563–575, https://doi.org/10.1007/s11661-017-4438-6.
[13] L.J. da Silva, D.M. Souza, D.B. de Araújo, R.P. Reis, A. Scotti, Concept and validation of an active cooling technique to mitigate heat accumulation in

WAAM, Int J Adv Manuf Technol 107 (5-6) (2020) 2513–2523, https://doi.org/10.1007/s00170-020-05201-4.
[14] X. Fang et al., "Correlations between Microstructure Characteristics and Mechanical Properties in 5183 Aluminium Alloy Fabricated by Wire-Arc Additive Manufacturing with Different Arc Modes," Materials (Basel, Switzerland), vol. 11, no. 11, 2018, doi: 10.3390/ma11112075.
[15] C. Su, X. Chen, C. Gao, Y. Wang, Effect of heat input on microstructure and mechanical properties of Al-Mg alloys fabricated by WAAM, Applied Surface Science 486 (2019) 431–440, https://doi.org/10.1016/j.apsusc.2019.04.255.
[16] K. Derekar, J. Lawrence, G. Melton, A. Addison, X. Zhang, L. Xu, M. Anis, B. Munir, Influence of Interpass Temperature on Wire Arc Additive Manufacturing (WAAM) of Aluminium Alloy Components, MATEC Web Conf. 269 (2019) 05001, https://doi.org/10.1051/matecconf/201926905001.
[17] C. Zhang, Y. Li, M. Gao, X. Zeng, Wire arc additive manufacturing of Al-6Mg alloy using variable polarity cold metal transfer arc as power source, Materials Science and Engineering: A 711 (2018) 415–423, https://doi.org/10.1016/j.msea.2017.11.084.
[18] Q. Wu, T. Mukherjee, A. De, T. DebRoy, Residual stresses in wire-arc additive manufacturing – Hierarchy of influential variables, Additive Manufacturing 35 (2020) 101355, https://doi.org/10.1016/j.addma.2020.101355.
[19] J. Gu, M. Gao, S. Yang, J. Bai, Y. Zhai, J. Ding, Microstructure, defects, and mechanical properties of wire + arc additively manufactured Al Cu4.3-Mg1.5 alloy, Materials & Design 186 (2020), https://doi.org/10.1016/j.matdes.2019.108357 108357.
[20] Y. Geng, I. Panchenko, X. Chen, Y. Ivanov, S. Konovalov, Investigation of Microstructure and Fracture Mechanism of Al-5.0Mg Alloys Fabricated by Wire Arc Additive Manufacturing, J. of Materi Eng and Perform 487 (5) (2021) 1366, https://doi.org/10.1007/s11665-021-05973-0.
[21] D. Ding, Z. Pan, D. Cuiuri, H. Li, A tool-path generation strategy for wire and arc additive manufacturing, Int J Adv Manuf Technol 73 (1–4) (2014) 173–183, https://doi.org/10.1007/s00170-014-5808-5.
[22] M.R. Dunlavey, Efficient polygon-filling algorithms for raster displays, ACM Transactions on Graphics 2 (4) (1983) 264–273.
[23] Y. Yehorov, L.J. da Silva, A. Scotti, Balancing WAAM Production Costs and Wall Surface Quality through Parameter Selection: A Case Study of an Al-Mg5 Alloy Multilayer-Non-Oscillated Single Pass Wall, JMMP 3 (2) (2019) 32, https://doi.org/10.3390/jmmp3020032.
[24] C. Zhang, C. Shen, X. Hua, F. Li, Y. Zhang, Y. Zhu, Influence of wire-arc additive manufacturing path planning strategy on the residual stress status in one single buildup layer, Int J Adv Manuf Technol 111 (3–4) (2020) 797–806, https://doi.org/10.1007/s00170-020-06178-w.
[25] V.T. Rajan, V. Srinivasan, K.A. Tarabanis, The optimal zigzag direction for filling a two-dimensional region, Rapid Prototyping Journal 7 (5) (2001) 231–241.
[26] X. Wang, A. Wang, Y. Li, A sequential path-planning methodology for wire and arc additive manufacturing based on a water-pouring rule, Int J Adv Manuf Technol 103 (9–12) (2019) 3813–3830, https://doi.org/10.1007/s00170-019-03706-1.
[27] F. Ren, Y. Sun, D. Guo, Combined reparameterization-based spiral toolpath generation for five-axis sculptured surface machining, Int J Adv Manuf Technol 40 (7–8) (2009) 760–768, https://doi.org/10.1007/s00170-008-1385-9.
[28] Y.i. Xiong, S.-I. Park, S. Padmanathan, A.G. Dharmawan, S. Foong, D.W. Rosen, G.S. Soh, Process planning for adaptive contour parallel toolpath in additive manufacturing with variable bead width, Int J Adv Manuf Technol 105 (10) (2019) 4159–4170, https://doi.org/10.1007/s00170-019-03954-1.
[29] C. Su, X. Chen, S. Konovalov, R. Arvind Singh, S. Jayalakshmi, L. Huang, Effect of Deposition Strategies on the Microstructure and Tensile Properties of Wire Arc Additive Manufactured Al-5Si Alloys, J. of Materi Eng and Perform 30 (3) (2021) 2136–2146, https://doi.org/10.1007/s11665-021-05528-3.
[30] S.W. Williams, F. Martina, A.C. Addison, J. Ding, G. Pardal, P. Colegrove, Wire + Arc Additive Manufacturing, Materials Science and Technology 32 (7) (2016) 641–647, https://doi.org/10.1179/1743284715Y.0000000073.
[31] I. Gibson, D. Rosen, B. Stucker, M. Khorasani (Eds.), Additive Manufacturing Technologies, Springer International Publishing, Cham, 2021.
[32] D. Radaj (Ed.), Heat Effects of Welding, Springer Berlin Heidelberg, Berlin, Heidelberg, 1992.
[33] Y. Ueda, H. Murakawa, N. Ma, Welding Deformation and Residual Stress Prevention, Elsevier Science, Burlington, 2012.
[34] P. Mercelis, J.-P. Kruth, Residual stresses in selective laser sintering and selective laser melting, Rapid Prototyping Journal 12 (5) (2006) 254–265, https://doi.org/10.1108/13552540610707013.
[35] A. Salmi, E. Atzeni, L. Iuliano, M. Galati, Experimental Analysis of Residual Stresses on AlSi10Mg Parts Produced by Means of Selective Laser Melting (SLM), Procedia CIRP 62 (2017) 458–463, https://doi.org/10.1016/j.procir.2016.06.030.
[36] L. Wang, X. Jiang, Y. Zhu, Z. Ding, X. Zhu, J. Sun, B. Yan, Investigation of Performance and Residual Stress Generation of AlSi10Mg Processed by Selective Laser Melting, Advances in Materials Science and Engineering 2018 (2018) 1–12, https://doi.org/10.1155/2018/7814039.
[37] P.A. Colegrove, H.E. Coules, J. Fairman, F. Martina, T. Kashoob, H. Mamash, L.D. Cozzolino, Microstructure and residual stress improvement in wire and arc additively manufactured parts through high-pressure rolling, Journal of Materials Processing Technology 213 (10) (2013) 1782–1791, https://doi.org/10.1016/j.jmatprotec.2013.04.012.
[38] J.R. Hönnige et al., Residual stress and texture control in Ti-6Al-4V wire + arc additively manufactured intersections by stress relief and rolling, Materials & Design 150 (7) (2018) 193–205, https://doi.org/10.1016/j.matdes.2018.03.065.
[39] J. Robinson, I. Ashton, P. Fox, E. Jones, C. Sutcliffe, Determination of the effect of scan strategy on residual stress in laser powder bed fusion additive manufacturing, Additive Manufacturing 23 (2018) 13–24, https://doi.org/10.1016/j.addma.2018.07.001.
[40] L. Sun, X. Ren, J. He, Z. Zhang, Numerical investigation of a novel pattern for reducing residual stress in metal additive manufacturing, Journal of Materials Science & Technology 67 (6) (2021) 11–22, https://doi.org/10.1016/j.jmst.2020.05.080.
[41] J. Goldak, A. Chakravarti, M. Bibby, A new finite element model for welding heat sources, Metall Trans B 15 (2) (1984) 299–305.
[42] J. Barrirero, C. Pauly, M. Engstler, J. Ghanbaja, N. Ghafoor, J. Li, P. Schumacher, M. Odén, F. Mücklich, Eutectic modification by ternary compound cluster formation in Al-Si alloys, Scientific reports 9 (1) (2019), https://doi.org/10.1038/s41598-019-41919-2.
[43] S. Pallaspuro, A. Kaijalainen, S. Mehtonen, J. Kömi, Z. Zhang, D. Porter, Effect of microstructure on the impact toughness transition temperature of direct-quenched steels, Materials Science and Engineering: A 712 (2018) 671–680, https://doi.org/10.1016/j.msea.2017.12.037.
[44] P. Lehto, H. Remes, T. Saukkonen, H. Hänninen, J. Romanoff, Influence of grain size distribution on the Hall-Petch relationship of welded structural steel, Materials Science and Engineering: A 592 (2014) 28–39, https://doi.org/10.1016/j.msea.2013.10.094.
[45] G. Langelandsvik, A. Horgar, T. Furu, H.J. Roven, O.M. Akselsen, Comparative study of eutectic Al-Si alloys manufactured by WAAM and casting, Int J Adv Manuf Technol 110 (3–4) (2020) 935–947, https://doi.org/10.1007/s00170-020-05735-7.
[46] A. Hadadzadeh, B. Shalchi Amirkhiz, A. Odeshi, J. Li, M. Mohammadi, Role of hierarchical microstructure of additively manufactured AlSi10Mg on dynamic loading behavior, Additive Manufacturing 28 (5) (2019) 1–13, https://doi.org/10.1016/j.addma.2019.04.012.
[47] H. Bian, K. Aoyagi, Y. Zhao, C. Maeda, T. Mouri, and A. Chiba, "Microstructure refinement for superior ductility of Al–Si alloy by electron beam melting," Additive Manufacturing, vol. 32, Part B, p. 100982, 2020, doi: 10.1016/j.addma.2019.100982